




# Spatial-Frequency Dual Domain Attention Network For Medical Image Segmentation

1<sup>st</sup> Zhenhuan Zhou 


College of Computer Science  
Nankai University  
Tianjin, China  
zhouzhenhuan@mail.nankai.edu.cn

2<sup>nd</sup> Along He 


College of Computer Science  
Nankai University  
Tianjin, China  
healong2020@163.com

3<sup>rd</sup> Yanlin Wu 


College of Computer Science  
Nankai University  
Tianjin, China  
1229145158@qq.com

4<sup>th</sup> Rui Yao 

The Department of Pediatric Dentistry  
Tianjin stomatological hospital  
Tianjin, China  
yaorui73@163.com

5<sup>th</sup> Xueshuo Xie\* 

Haihe Lab of ITAI  
Tianjin, China  
xueshuoxie@nankai.edu.cn

6<sup>th</sup> Tao Li\* 

College of Computer Science  
Nankai University and  
Haihe Lab of ITAI  
Tianjin, China  
litao@nankai.edu.cn

**Abstract**—In medical images, various types of lesions often manifest significant differences in their shape and texture. Accurate medical image segmentation demands deep learning models with robust capabilities in multi-scale and boundary feature learning. However, previous networks still have limitations in addressing the above issues. Firstly, previous networks simultaneously fuse multi-level features or employ deep supervision to enhance multi-scale learning. However, this may lead to feature redundancy and excessive computational overhead, which is not conducive to network training and clinical deployment. Secondly, the majority of medical image segmentation networks exclusively learn features in the spatial domain, disregarding the abundant global information in the frequency domain. This results in a bias towards low-frequency components, neglecting crucial high-frequency information. To address these problems, we introduce SF-UNet, a spatial-frequency dual-domain attention network. It comprises two main components: the Multi-scale Progressive Channel Attention (MPCA) block, which progressively extract multi-scale features across adjacent encoder layers, and the lightweight Frequency-Spatial Attention (FSA) block, with only 0.05M parameters, enabling concurrent learning of texture and boundary features from both spatial and frequency domains. We validate the effectiveness of the proposed SF-UNet on three public datasets. Experimental results show that compared to previous state-of-the-art (SOTA) medical image segmentation networks, SF-UNet achieves the best performance, and achieves up to 9.4% and 10.78% improvement in DSC and IOU. Codes will be released at <https://github.com/nkicsl/SF-UNet>.

**Index Terms**—Medical Image Segmentation, Multi-scale Feature, Frequency Domain Attention, CNN, Deep Learning

## I. INTRODUCTION

Medical image segmentation is the essential task and prerequisite for computer-aided diagnosis [1]. It refers to assigning each pixel a corresponding label to identify tissues or lesions. Deep learning-based medical image segmentation methods improve the segmentation accuracy, significantly reducing the workload of experts and eliminating the subjectivity of manual

annotation. For example, segmenting lesions in fundus images and dermoscopic images enables early screening and intervention for diabetic retinopathy [2] and can enhance the diagnostic efficiency of melanoma and improve patient survival rates [3]. Accurate segmentation of teeth in CBCT images is also an important prerequisite for computer-aided diagnosis in oral medicine [4] [5]. These cases all highlight the significant role of deep learning in medical image segmentation.

Convolutional Neural Networks (CNN) have been widely used in computer vision tasks due to their powerful feature extraction capabilities. In medical image segmentation, UNet [6] and its variants [7] [8] are representative deep learning networks and have achieved remarkable performances. However, such CNN segmentation models still have some limitations: Firstly, due to the limitation of kernel size, CNN often have a limited receptive field, lacking the ability to learn global information and long-range relationships. Although some large kernel convolutional networks [9] [10] have been proposed recently, they often require more computational resources. Secondly, in medical image segmentation, the multi-scale problem is a significant challenge because different types of lesions often exhibit large differences in shape and volume [11]. CNN-based encoders often gradually downsample the resolution of feature maps, which may lead to the neglect of some small lesions, causing semantic loss and ultimately affecting the reliability of segmentation results. Some works use deep supervision [12] or fuse features from all levels of the encoder [13] to enhance the network’s multi-scale capabilities, but these may still lead to significant computational overhead and feature redundancy.

Transformer was originally proposed in natural language processing [14] and quickly applied to computer vision [15]. For medical images, global information and long-range relationship are crucial [16] [17]. Some pure transformer [18] [19] and hybrid transformer networks [20] [21] have achieved

The corresponding authors: Xueshuo Xie\* and Tao Li\*

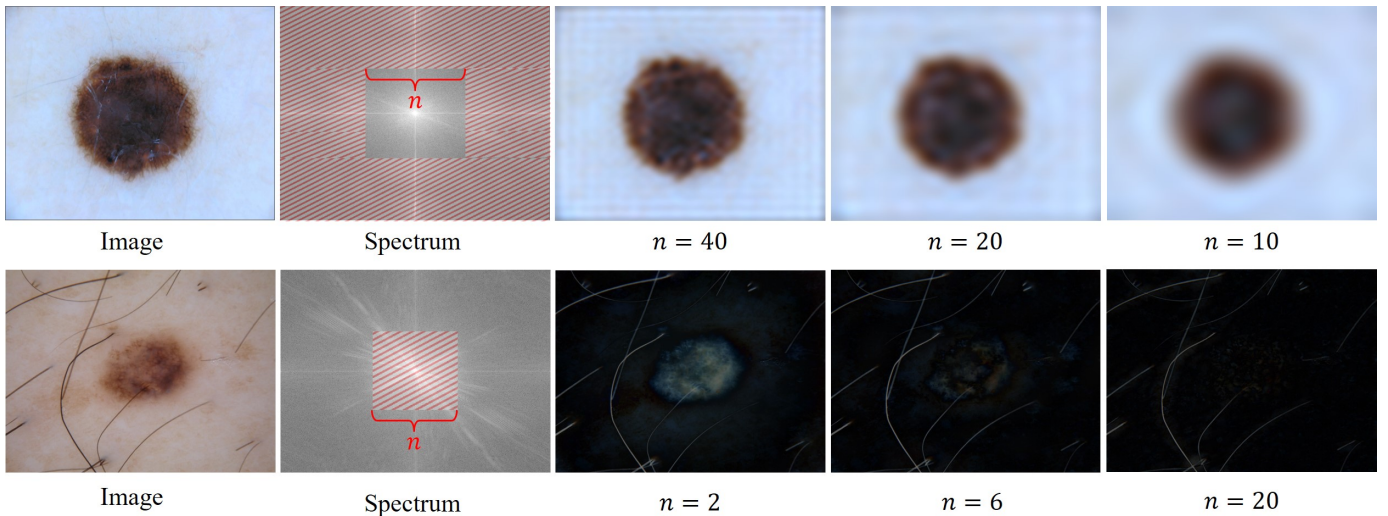


Fig. 1. This figure illustrates the impact of high-frequency and low-frequency components on the image content from the ISIC2018 dataset. The top and bottom rows represent gradually removing the high-frequency and low-frequency features with different filter sizes of the image, respectively. Here  $n$  represents the width of the filter and the red slashed area represents the removed spectrum.

good results in medical image segmentation. However, transformers are not without their flaws. On one hand, global self-attention has quadratic computational complexity, leading to larger computational overhead and data requirements compared to CNN [22]. On the other hand, some researches have shown that global self-attention primarily focuses on the low-frequency components of the image, potentially neglecting high-frequency information to some extent [23]. Low-frequency components correspond to the content and texture of the image, while high-frequency components correspond to the edges and details [24]. As shown in Fig. 1, in the first row, we gradually extract the high-frequency information of the image, it can be observed that the image becomes increasingly blurred with the reduction of details. In the second row, as we gradually extract the low-frequency information from the image, we can observe that the texture of the image is removed, leaving only the components with larger gradients such as hair or boundaries. Therefore, to achieve accurate segmentation results, the network should consider both low-frequency and high-frequency information, ensuring the integrity of texture, boundaries and details.

To solve the problems mentioned above, we proposed a U-shaped Spatial-Frequency Dual Domain Attention Network, named SF-UNet. It consists of two main blocks: the Multi-scale Progressive Channel Attention (MPCA) block progressively fuses features from adjacent levels of the encoder to generate cross-scale channel attention maps, enhancing the network’s ability to learn multi-scale features and avoiding feature redundancy. The Frequency-Spatial Attention (FSA) block consists of two branches. One of them learns attention maps in the spatial domain, and the other branch applies 2D Discrete Fourier Transformation to the spatial feature maps, and then separating the frequency feature maps into high-frequency and low-frequency components. In the low-frequency component, we use a learnable filter to adaptively

adjust the weights of each frequency component, enabling global feature learning from a holistic perspective. Finally, we restore the original high-frequency components of the feature maps to the filtered low-frequency components, aiming to preserve the integrity of high-frequency details in the decoders. We validated the proposed method on three public datasets, and the results demonstrate that SF-UNet can outperform previous SOTA medical image segmentation models.

Our contributions are summarized as follows:

- We design the MPCA and FSA block, the former can effectively learn multi-scale channel features, while the latter simultaneously conducts feature learning in both spatial and frequency domains, preserving the integrity of high-frequency information while retaining the ability to learn global information.
- Based on MPCA and FSA, we built a U-shaped Spatial-Frequency Dual Domain Attention Network with strong capability to capture multi-scale features. Unlike Transformers, it ensures the network’s global feature learning ability from the frequency domain and preserves high-frequency detail features.
- Extensive experiments were conducted on three public datasets to validate the effectiveness of the proposed network. The results show that SF-UNet can outperform previous SOTA networks. We also conducted ablation studies to further demonstrate the effectiveness of each proposed block.

## II. METHOD

### A. Overall Structure

The overall pipeline of SF-UNet is illustrated in Fig 2. The encoder of SF-UNet consists of four encoder blocks followed by a bottleneck layer, following the implementation of VGG16 [25]. The encoder and decoder in SF-UNet are accompanied by MPCA and FSA blocks. Specifically, given

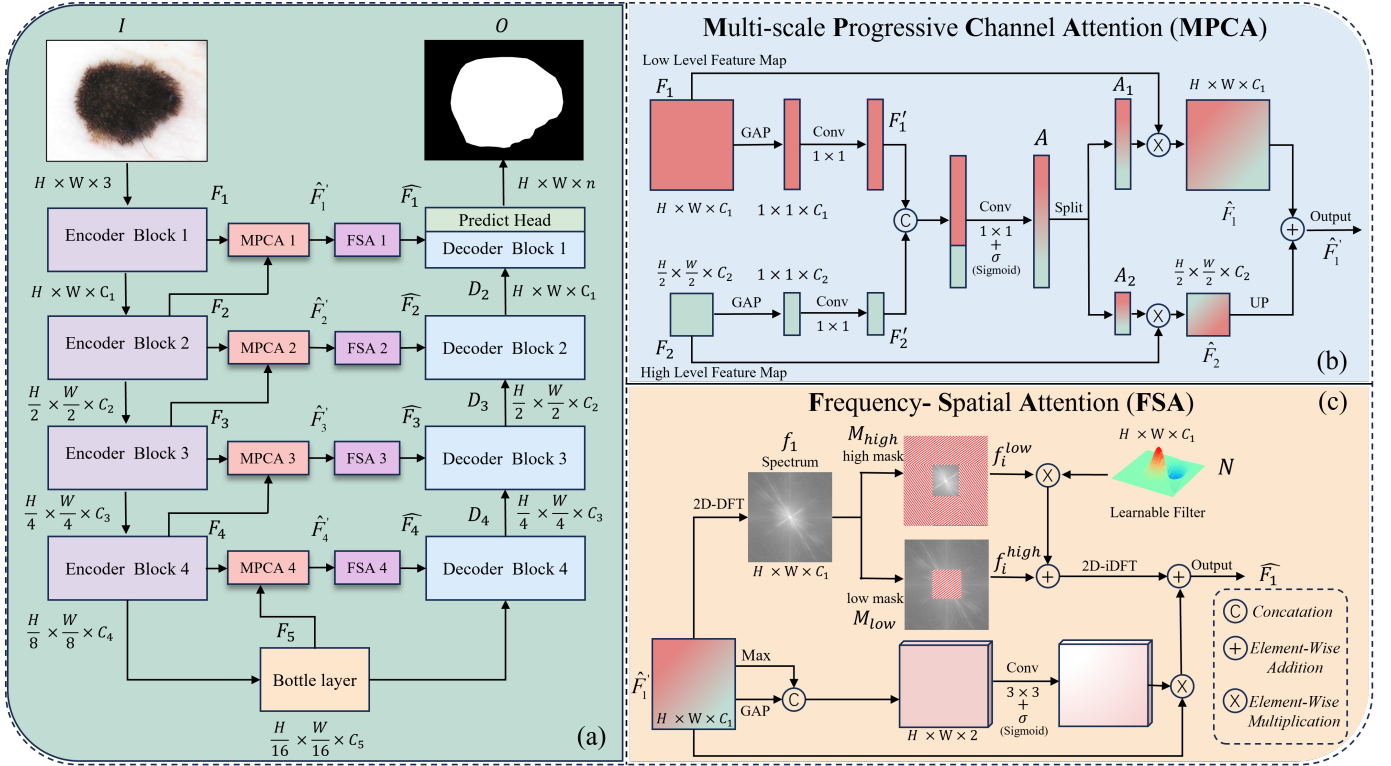


Fig. 2. The overall architecture of the proposed network and detailed structures of each block. (a) the overall structure of SF-UNet, (b) the structure of MPCA. (c) the structure of FSA. 2D-DFT stands for 2D Discrete Fourier Transform, and 2D-IDFT stands for 2D Inverse Discrete Fourier Transform.

an image  $I \in \mathbb{R}^{H \times W \times C}$ ,  $H$ ,  $W$  and  $C$  represent the height, width and channel numbers of the image, respectively. First, the output features of four encoder blocks and bottle layer are denoted as  $F_i \in \mathbb{R}^{\frac{H}{2^{i-1}} \times \frac{W}{2^{i-1}} \times C_i}$ , where  $i \in \{1, 2, 3, 4\}$ , respectively. Then, for each level of MPCA block,  $F_i$  and  $F_{i+1}$  are used as inputs to accomplish cross-scale channel feature learning. The output of each MPCA block will go through a corresponding FSA block for spatial and frequency dual domain feature learning. Finally, a prediction head is used to get the final segmentation result  $O$ . Next, we elaborate the proposed MPCA and FSA blocks, respectively.

### B. Multi-scale Progressive Channel Attention block

1) **Motivation:** The multi-scale challenge in medical image segmentation is prominent. To ensure that each decoder block possesses cross-scale feature information and avoids feature redundancy, we propose the MPCA block. It progressively integrates feature maps from the current scale and the next scale to enhance the network's multi-scale feature learning capability. The MPCA block fuse multi-scale features in two aspects. First, it generates channel attention maps from two adjacent scales simultaneously. Second, at the output of the MPCA block, we merge the weighted feature maps of the current scale and the next scale. This ensures that the outputs of the MPCA blocks include multi-scale fused features.

2) **Structure Detail:** The detailed structure of MPCA block (using MPCA 1 as an example) is illustrated in Fig 2 (b). Each MPCA block has two inputs, i.e., the current and next encoder

output feature maps  $F_i$  and  $F_{i+1}$ , respectively. Then the  $F_i$  and  $F_{i+1}$  will go through two independent Global Average Pooling (GAP) and  $1 \times 1$  convolutional layers for dimension reduction and feature extraction before being concatenated. Finally, another  $1 \times 1$  convolutional layer will be used to fuse the two feature maps, obtaining the multi-scale channel attention map  $A$ . It can be defined by the following Eq. 1 and 2:

$$F'_{i+1} = \text{Conv}_{1 \times 1}(\text{GAP}(F_{i+1})) \quad (1)$$

$$A = \sigma(\text{Conv}_{1 \times 1}(\text{Concate}(F'_i, F'_{i+1}))) \quad (2)$$

where  $\text{Conv}_{1 \times 1}$  denotes the  $1 \times 1$  convolutional layers and  $\text{Concate}$  denotes concatenation along channel dimension.  $A$  fused the channel features from two adjacent scales and completed cross-scale information exchange. Next, we split  $A$  into two parts,  $A_i$  and  $A_{i+1}$ , and dimensions are consistent with  $F_i$  and  $F_{i+1}$ . Subsequently,  $F_i$  and  $F_{i+1}$  will be multiplied by the corresponding  $A_i$  and  $A_{i+1}$  to obtain the weighted feature maps  $\hat{F}_i$  and  $\hat{F}_{i+1}$ . We use a transposed convolutional layer to upsample the feature map  $\hat{F}_{i+1}$  by a factor of 2 and match the channel number with  $\hat{F}_i$ , resulting in  $\hat{F}'_{i+1}$ . Finally, we perform element-wise addition between  $\hat{F}_i$  and  $\hat{F}'_{i+1}$  to achieve feature fusion and obtain  $\hat{F}'_i$ , which serves as the output of the MPCA block and the input of the FSA block. The above process can be represented by the following Eq.3, 4 and 5. We will introduce the structure of FSA block in the next section.

$$A_i, A_{i+1} = \text{Split}(A) \quad (3)$$

$$F_{i(+1)}^{\hat{}} = F_{i(+1)} \otimes A_{i(+1)} \quad (4)$$

$$\hat{F}'_i = \hat{F}_i \oplus \text{UP}(\hat{F}_{i+1}) \quad (5)$$

Here,  $\otimes$  and  $\oplus$  represent element-wise multiplication and addition, respectively. UP denotes the transposed convolutional layer.

### C. Frequency-Spatial Attention block

1) **Motivation:** In medical imaging, the high-frequency information hold paramount importance for accurate diagnosis, as they encapsulate the precise delineation and boundaries of lesions. This underscores the need for meticulous consideration of high-frequency features inherent in medical images. Our objective is to equip the network with global feature learning capabilities, while conserving the high-frequency characteristics of the images. Based on this, we propose the FSA block. Unlike previous works [26]–[28] that solely rely on spatial domain processing, the FSA block concurrently conducts feature learning in both frequency and spatial domains. Specifically, the FSA block operates on the input feature maps by processing them with frequency and spatial branches. In the frequency branch, the spatial features are transformed into the frequency domain using 2D Discrete Fourier Transform (DFT), and the low-frequency and high-frequency components are separated. Subsequently, a learnable filter is applied to the low-frequency component for adaptive feature learning from a global perspective. The original high-frequency components are then reintegrated with the filtered low-frequency components, and the resultant spatial domain features are obtained using 2D Inverse Discrete Fourier Transform (IDFT). Meanwhile, in the spatial branch, spatial domain feature learning is facilitated using a spatial attention block adapted from [29]. Finally, the outputs from the two branches are fused to generate the output of the FSA block.

2) **Structure Detail:** The detailed structure of FSA block (using FSA 1 as an example) is illustrated in Fig 2 (c). Given the output  $\hat{F}'_i \in \mathbb{R}^{H \times W \times C_1}$  of MPCA block, we initially convert it into the frequency domain using the 2D DFT as depicted in Eq. 6. Here,  $f_i \in \mathbb{R}^{H \times W \times C_1}$  represents the frequency domain feature maps,  $\hat{F}'_i(x, y)$  denotes the pixel values of the original features in the spatial domain, H and W denote the height and width of the feature maps, respectively.

$$f_i(U, V) = \sum_{x=0}^{H-1} \sum_{y=0}^{W-1} \hat{F}'_i(x, y) e^{-j2\pi(\frac{Ux}{H} + \frac{Vy}{W})} \quad (6)$$

Then, we separate the frequency features into high-frequency  $f_i^{high}$  and low-frequency  $f_i^{low}$ . This is achieved with two masks,  $M_{low} \in \mathbb{R}^{H \times W \times 1}$  and  $M_{high} \in \mathbb{R}^{H \times W \times 1}$ . For  $M_{low}$ , a square of side length  $n$  is centered in the mask and assigned a value of 1, while the remaining regions are assigned a value of 0. Then, we perform element-wise multiplication between  $f_i$  and  $M_{low}$  to obtain the low-frequency component  $f_i^{low}$ , as defined in Eq. 7. For  $M_{high}$ , the small square area is assigned a value of 0 and the rest is assigned to 1. We then perform element-wise multiplication between  $f_i$  and  $M_{high}$

to obtain the high-frequency component  $f_i^{high}$ , as depicted in Eq. 8. In Fig 2 (c), red diagonal lines are used to visually represent the regions assigned a value of 0.

$$f_i^{low} = f_i \otimes M_{low} \quad (7)$$

$$f_i^{high} = f_i \otimes M_{high} \quad (8)$$

Subsequently, for  $f_i^{low}$ , we apply an adaptive learnable global filter  $N \in \mathbb{R}^{H \times W \times C_1}$  to perform filtering. Then, we reintegrate the original high-frequency feature  $f_i^{high}$  with the filtered  $f_i^{low'}$ , resulting in the spectrum  $f'_i$  after global learning and feature fusion, as depicted in Eq. 9. Following this, a 2D IDFT is employed, as defined in Eq. 10, to obtain the spatial domain feature  $\hat{F}''_i$ .

$$f'_i = f_i^{high} \oplus (f_i^{low} \otimes N) \quad (9)$$

$$\hat{F}''_i(x, y) = \frac{1}{HW} \sum_{U=0}^{H-1} \sum_{V=0}^{W-1} f'_i(U, V) e^{j2\pi(\frac{Ux}{H} + \frac{Vy}{W})} \quad (10)$$

Meanwhile, for the output  $\hat{F}'_i$  from MPCA, we also use the spatial attention (SA) [29] within the spatial branch to facilitate feature learning. The final output of the FSA block can be obtained as follows:

$$\hat{F}_i = \hat{F}''_i \oplus SA(\hat{F}'_i) \quad (11)$$

### D. Decoder blocks

In each decoder block, we employ linear interpolation to upsample the feature maps by a factor of 2. Subsequently, we concatenate the high-resolution feature map with the upsampled feature maps along the channel dimension. Then, the concatenated feature maps undergo two  $3 \times 3$  convolutional layers to complete feature fusion and learning. Each convolutional layer followed by a ReLU activation function, enhancing the network's nonlinear learning capability. The entire process can be defined by Eq. 12. It is important to note that  $D_1$  passes through a prediction head consisting of two  $3 \times 3$  convolutional layers to obtain the final segmentation result  $O \in \mathbb{R}^{H \times W \times n}$ , where H and W represent the height and width of the image, respectively, and n represents the number of classes.

$$D_i = \text{Relu}(\text{Conv}(\text{Concat}(\hat{F}_i, \text{UP}(\hat{F}_{i+1})))) \quad i \in (1, 2, 3, 4) \quad (12)$$

## III. EXPERIMENTS

### A. Datasets

1) **ISIC-2018** [30]: The ISIC-2018 segmentation dataset developed by the International Skin Imaging Collaboration (ISIC), and it is employed for skin lesion segmentation. This dataset comprises 2594 training images, 100 validation images, and 1000 test images. Each image is captured using professional dermatoscopic equipment and annotated by experts. For our experiments, we use the official training, validation, and test sets provided by ISIC.

2) **BUSI** [31]: The Breast Ultrasound Image Dataset (BUSI) consists of 647 breast ultrasound images from different patients, including 437 images of benign tumors and 210 images of malignant tumors. For our experiments, we randomly divide them into training (487 images), validation (80 images), and test sets (80 images).

3) **NKUT** [32]: NKUT is a 3D CBCT dataset used for pediatric mandibular wisdom tooth germ segmentation and it consists of 133 CBCT scans. Each data is carefully annotated at the pixel level by two experts for the mandibular wisdom teeth (MWT), second molars (SM), and the surrounding alveolar bone (AB). In our experiment, we adopt the same preprocessing methods outlined in [32]. Finally, we randomly divided the acquired images into training set (17251 images), validation set (1450 images), and test set (2058 images).

### B. Implementation details

In our experiments, we applied data augmentations, including random horizontal flipping, random vertical flipping and random rotation. To ensure fairness, all models were trained using the same strategies. We used the Adam [33] optimizer with an initial learning rate of 0.0001, which was decayed using the ‘‘Poly’’ strategy. The number of epochs was set to 200 and the loss functions was a combination of cross-entropy and Dice loss [34]. The channel numbers for the four encoder blocks were set to [64, 128, 256, 512]. For all datasets, we resized the images and labels to  $224 \times 224$ . Model parameters were randomly initialized without leveraging any pre-trained weights. For all models, we selected the weights achieving the top three IoU scores on the validation set for testing on the test set, and retain the best result. Our framework was implemented using Pytorch, all experiments were conducted on two NVIDIA GeForce RTX 3090 GPUs.

### C. Experimental results

To comprehensively evaluate the performance of SF-UNet, we conducted qualitative and quantitative experiments on three datasets, comparing against seven previous SOTA networks: UNet [6], PSPNet [35], DeepLabV3+ [36], TransUNet [20], Swin-UNet [37], ACC-UNet [13], and MGFuseSeg [38].

1) **Results on ISIC-2018**: Dermoscopy images present typical challenges with multi-scale issue and blurry boundaries [39]. Skin diseases vary greatly in size and texture, demanding networks to capture both low-level and high-level features. Moreover, the boundaries between skin lesions and normal skin often lack clarity, presenting a significant challenge in lesion boundary delineation. Table I shows the quantitative results on the ISIC-2018 dataset. It is evident that SF-UNet outperformed previous SOTA networks in terms of DSC and IOU on the test set, highlighting the robust multi-scale feature learning and boundary feature learning capabilities of SF-UNet.

Fig 3 presents the qualitative results on the ISIC-2018 dataset. It is visually apparent that SF-UNet produces segmentation results with the smoothest and clearest boundaries,

TABLE I  
THE QUANTITATIVE EXPERIMENTAL RESULTS ON THE ISIC-2018 DATASET, PARAMS DENOTES THE NUMBERS OF PARAMETER. THE BOLD RESULTS INDICATE THE BEST PERFORMANCE, AND UNDERLINED RESULTS INDICATE THE SECOND BEST.

Dataset	Model	#Params	Source & Year	DSC(%) $\uparrow$	IOU(%) $\uparrow$
ISIC-2018	UNet [6]	24.89M	MICCAI 2015	87.93	80.34
	DeepLabV3+ [14]	20.15M	ECCV 2018	88.17	80.67
	PSPNet [35]	16.16M	CVPR 2017	87.81	80.26
	TransUNet [20]	92.23M	ArXiv 2021	<u>88.27</u>	<u>81.27</u>
	Swin-UNet [37]	27.15M	ECCV 2022	87.74	80.13
	ACC-UNet [13]	16.77M	MICCAI 2023	87.81	80.45
	MGFuseSeg [38]	22.27M	BIBM 2023	87.76	80.43
	SF-UNet (ours)	28.89M	/	<b>88.46</b>	<b>81.34</b>

closely resembling the ground truth. In contrast, The segmentation results of other networks display problems such as loss of texture details or boundary confusion. The results highlights the effectiveness of SF-UNet and preserves high-frequency features from a frequency-domain perspective to generate accurate segmentation results.

2) **Results on BUSI**: Table II displays the quantitative results on the BUSI dataset. It can be observed that SF-UNet achieved the best performance in terms of HD95, DSC, and IOU, surpassing the previous SOTA networks. Compared to the second-best ACC-UNet, it improves the results by 0.64%, 0.42%, and 0.76% respectively. This demonstrates that SF-UNet exhibits high robustness, achieving excellent generalization performance even on small datasets.

TABLE II  
THE QUANTITATIVE RESULTS ON THE BUSI DATASET, PARAMS DENOTES THE NUMBERS OF PARAMETER. THE BOLD RESULTS INDICATE THE BEST PERFORMANCE, AND UNDERLINED RESULTS INDICATE THE SECOND BEST.

Dataset	Model	#Params	HD95 $\downarrow$	DSC(%) $\uparrow$	IOU(%) $\uparrow$
BUSI	UNet [6]	24.89M	101.79	73.27	64.30
	DeepLabV3+ [14]	20.15M	101.13	74.74	65.17
	PSPNet [35]	16.16M	80.67	72.82	63.24
	TransUNet [20]	92.23M	97.91	74.89	66.35
	Swin-UNet [37]	27.15M	112.34	66.66	56.42
	ACC-UNet [13]	16.77M	<u>80.17</u>	<u>75.64</u>	<u>66.44</u>
	MGFuseSeg [38]	22.27M	113.62	67.69	57.52
	SF-UNet (ours)	28.89M	<b>79.53</b>	<b>76.06</b>	<b>67.20</b>

Fig 4 presents the qualitative results and it is evident that among all networks, SF-UNet achieves segmentation results with more accurate and clear boundaries. Other networks display issues such as boundary missing or excessive smoothness, along with inaccurate lesion detection. This further demonstrates the importance of the MPCA and FSA blocks, which enable the network to accurately learn texture features of lesions at multiple scales and precisely capture high-frequency boundary features, leading to better segmentation performance.

3) **Results on NKUT**: As mentioned in [32], the challenge of the NKUT dataset are the multi-scale and semantic confusion problems. This is because children’s mandibular wisdom teeth germs are often small and can be easily overlooked during the progressive downsampling. Additionally, determining the boundary between teeth and alveolar bone also poses a

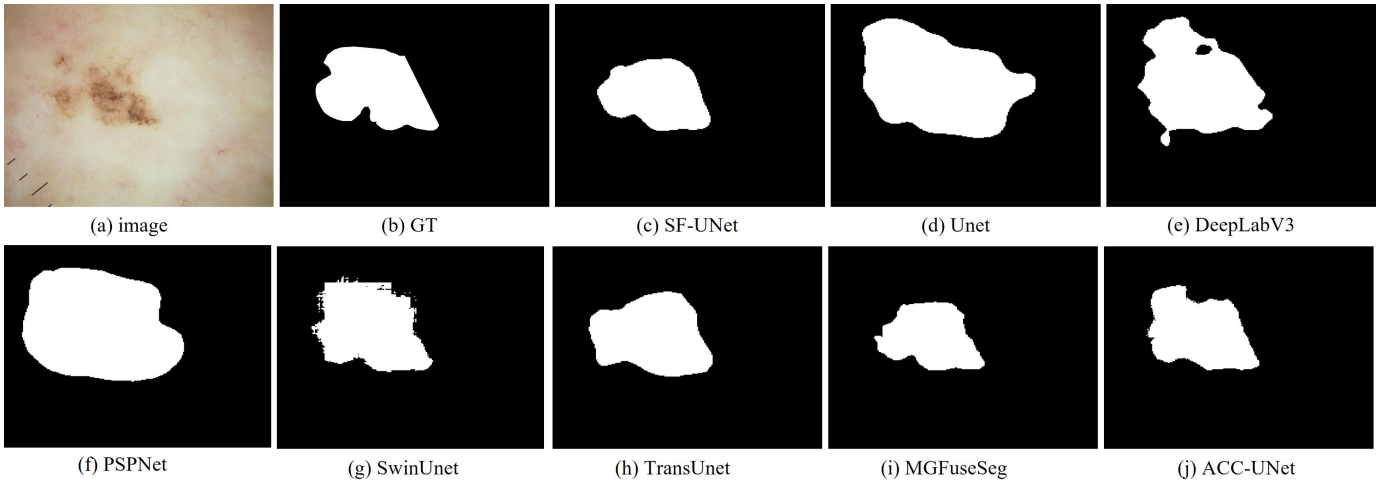


Fig. 3. Qualitative results on ISIC-2018 dataset. (a) represents the original image and (b) represents the corresponding ground truth. Black represents the background, i.e., normal skin, while white represents lesions. It can be observed that SF-UNet achieves the best performance.

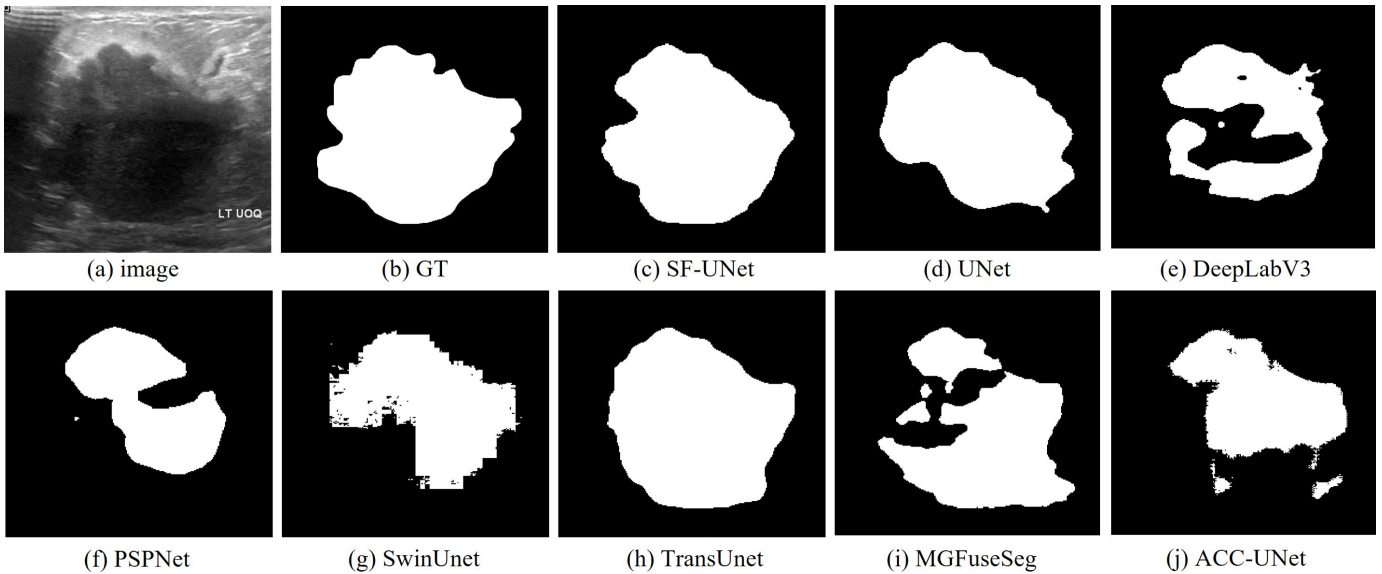


Fig. 4. Qualitative results on BUSI dataset. (a) represents the original image and (b) represents the corresponding ground truth. Black represents the background, while white represents tumors. It can be observed that SF-UNet achieves the best performance.

significant challenge. Addressing these concerns necessitates the network with robust multi-scale and edge feature learning capabilities. Table III presents the quantitative results on the NKUT dataset. From the results, SF-UNet achieved the best performance in terms of AB and average performance, and achieved the second best performance in terms of MWT and SM. For TransUNet, despite outperforming SF-UNet in the segmentation of MWT and SM, it has two limitations. Firstly, its parameters (92.23M) are significantly higher than SF-UNet. Secondly, its performance in segmenting AB is subpar, indicating inadequate multi-scale and boundary information learning capabilities. Its high IOU in MWT and SM may stem from aggressive classification of ambiguous boundaries between teeth and bones as teeth, compromising AB accuracy to enhance MWT and SM accuracy. Therefore, considering these aspects comprehensively, SF-UNet remains competitive.

TABLE III  
THE QUANTITATIVE EXPERIMENTAL RESULTS ON THE NUKT DATASET, WE CHOSE IOU AS THE EVALUATION METRIC. MWT REPRESENTS THE MANDIBULAR WISDOM TOOTH GERM, SM INDICATES THE SECOND MANDIBULAR MOLAR, AND AB REPRESENTS THE ALVEOLAR BONE. THE BOLD RESULTS INDICATE THE BEST PERFORMANCE, AND UNDERLINED RESULTS INDICATE THE SECOND BEST.

Dataset	Model	MWT	SM	AB	Mean
NKUT	UNet [6]	84.61	81.61	53.56	73.26
	DeepLabV3+ [14]	85.54	84.86	52.97	74.46
	PSPNet [35]	83.91	82.17	42.37	69.48
	TransUNet [20]	<b>88.37</b>	<b>83.76</b>	51.79	<u>74.64</u>
	Swin-UNet [37]	81.12	76.78	<u>55.01</u>	70.97
	ACC-UNet [13]	85.61	83.07	53.43	74.04
	MGFuseSeg [38]	86.02	81.09	53.41	73.51
	SF-UNet (ours)	<u>86.15</u>	<u>82.59</u>	<b>56.27</b>	<b>75.00</b>

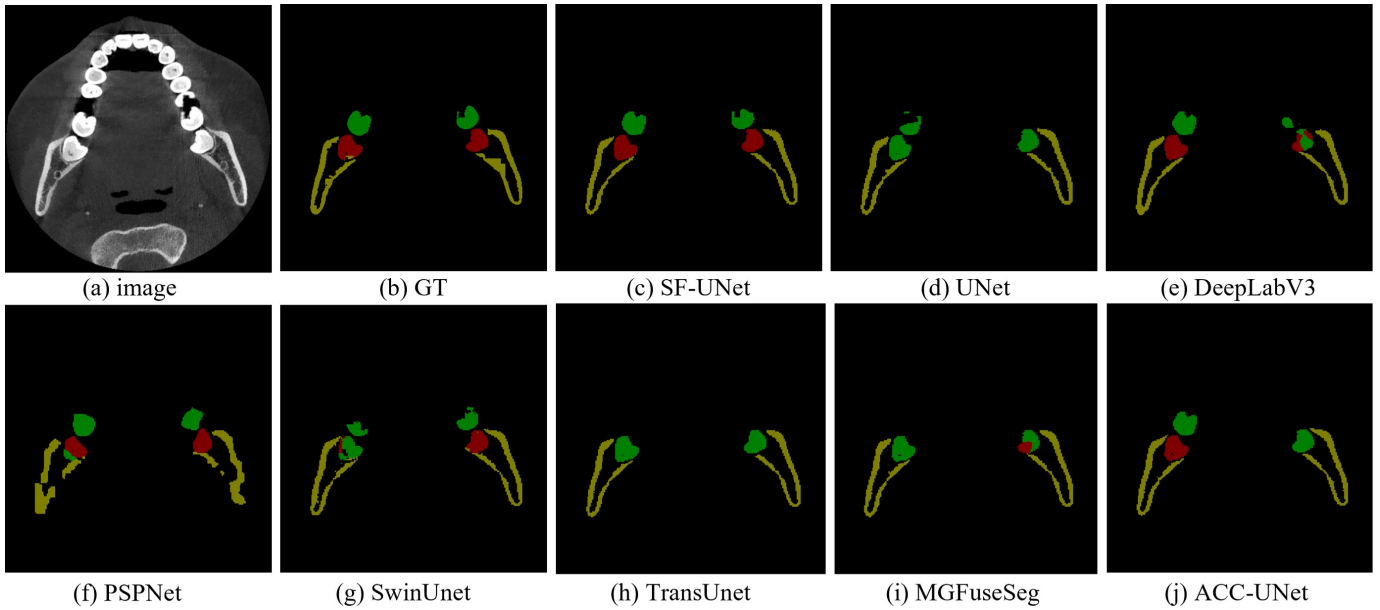


Fig. 5. Qualitative results on NKUT dataset. (a) represents the original image and (b) represents the corresponding ground truth. Red represents Mandibular Wisdom Teeth (MWT), green represents Second Molars (SM), and yellow represents Alveolar Bone (AB).

Fig 5 illustrates the qualitative results on the NKUT dataset. We can observe that SF-UNet can effectively delineate MWT, SM, and AB, demonstrating clear boundaries between teeth and bone. Despite the extreme morphological similarity between the MWT and SM in the image, SF-UNet accurately distinguishes between them. This demonstrates that SF-UNet effectively learns deep and high-level features. In contrast, other networks display various issues, including missing teeth, ambiguous teeth, omitted bone structures, or unclear boundaries between teeth and bone.

#### D. Ablation studies

We conducted ablation studies of SF-UNet on the BUSI dataset to validate the effectiveness of the proposed MPCA and FSA blocks. In the second row of Tabel IV, it can be observed that integrating the FSA block into the backbone UNet leads to improvements in both DSC and IOU, with increases of 0.83% and 0.81% , respectively. Meanwhile, the parameters are only increased by 0.05M, demonstrating the the lightweight and effectiveness of the FSA block. In the third row of the Tabel IV, the ntegration of only the MPCA block to the backbone results in significant enhancements in both DSC and IOU, increasing by 2.24% and 3.17%, respectively. This underscores the multi-scale learning capability of MPCA, substantially bolstering the network’s robustness and effectiveness in addressing multi-scale lesion segmentation challenges. In the last row of Table IV, upon integrating both MPCA and FSA into the backbone, the SF-UNet is formed, achieving the best performance in both DSC and IOU, with improvements of 2.79% and 2.9%, respectively, compared to the backbone UNet. This demonstrates the complementary nature of MPCA and FSA, indicating that both of them are indispensable.

TABLE IV

THIS TABLE SHOWS THE ABLATION EXPERIMENT RESULTS OF SF-UNET ON THE BUSI DATASET, WHERE  $\times$  INDICATES THE BLOCK IS NOT INCLUDED, AND  $\checkmark$  INDICATES THE BLOCK IS INCLUDED. WE CHOSE DSC AND IOU AS THE EVALUATION METRICS.

Backbone	MPCA	FSA	DSC	IOU	Params
	$\times$	$\times$	73.27	64.30	24.89M
UNet [6]	$\times$	$\checkmark$	74.10	65.11	24.94M
	$\checkmark$	$\times$	75.51	67.47	28.84M
	$\checkmark$	$\checkmark$	<b>76.06</b>	<b>67.20</b>	28.89M

#### IV. CONCLUSION

In this paper, we proposed SF-UNet for medical image segmentation, which consists of two blocks: MPCA and FSA blocks. We conducted extensive experiments on three public datasets, and the results showed that SF-UNet achieved the best performance, surpassing previous SOTA networks. Compared to other networks, SF-UNet demonstrated superior accuracy in segmenting textures and boundaries, as well as in distinguishing between various lesion types and sizes. Furthermore, we conducted ablation studies, providing quantitative results that validate the efficacy of all proposed blocks. In the future, we will continue to explore frequency-domain-based segmentation methods to achieve efficient, accurate, and computationally less intensive medical image segmentation, thereby establishing a robust framework for computer-aided diagnosis.

#### ACKNOWLEDGMENT

This work is partially supported by the National Natural Science Foundation (62272248), the Natural Science Foundation of Tianjin (23JCZDJC01010, 23JCQNJC00010).

## REFERENCES

- [1] J. Li, S. Chen, S. Ma, F. Guo, and J. Tang, "Mixunet: Mix the 2d and 3d models for robust medical image segmentation," in *2023 IEEE International Conference on Bioinformatics and Biomedicine (BIBM)*, pp. 1242–1247, IEEE, 2023.
- [2] T. Li, Y. Gao, K. Wang, S. Guo, H. Liu, and H. Kang, "Diagnostic assessment of deep learning algorithms for diabetic retinopathy screening," *Information Sciences*, vol. 501, pp. 511–522, 2019.
- [3] S. Ren and Y. Peng, "Mff-net: Multiscale feature fusion network for skin lesion segmentation," in *2023 IEEE International Conference on Bioinformatics and Biomedicine (BIBM)*, pp. 3473–3479, IEEE, 2023.
- [4] W. Cui, Y. Wang, Q. Zhang, H. Zhou, D. Song, X. Zuo, G. Jia, and L. Zeng, "Ctooth: a fully annotated 3d dataset and benchmark for tooth volume segmentation on cone beam computed tomography images," in *International Conference on Intelligent Robotics and Applications*, pp. 191–200, Springer, 2022.
- [5] Z. Zheng, H. Yan, F. C. Setzer, K. J. Shi, M. Mupparapu, and J. Li, "Anatomically constrained deep learning for automating dental cbct segmentation and lesion detection," *IEEE Transactions on Automation Science and Engineering*, vol. 18, no. 2, pp. 603–614, 2020.
- [6] O. Ronneberger, P. Fischer, and T. Brox, "U-net: Convolutional networks for biomedical image segmentation," in *Medical image computing and computer-assisted intervention—MICCAI 2015: 18th international conference, Munich, Germany, October 5-9, 2015, proceedings, part III 18*, pp. 234–241, Springer, 2015.
- [7] J. Qin, X. He, J. Yu, W. Zhang, J. Xiang, and L. Wu, "Aia-unet: Attention in attention for medical image segmentation," in *2023 IEEE International Conference on Bioinformatics and Biomedicine (BIBM)*, pp. 2179–2182, IEEE, 2023.
- [8] Q. Wang, J. Wu, Y. Wang, H. Qu, S. Nie, and H. Yang, "Lde-unet: A novel model for rapid covid-19 diagnosis via ct image segmentation," in *2023 IEEE International Conference on Bioinformatics and Biomedicine (BIBM)*, pp. 2273–2276, IEEE, 2023.
- [9] M.-H. Guo, C.-Z. Lu, Z.-N. Liu, M.-M. Cheng, and S.-M. Hu, "Visual attention network," *Computational Visual Media*, vol. 9, no. 4, pp. 733–752, 2023.
- [10] R. Azad, L. Niggemeier, M. Hüttemann, A. Kazerouni, E. K. Aghdam, Y. Velichko, U. Bagci, and D. Merhof, "Beyond self-attention: Deformable large kernel attention for medical image segmentation," in *Proceedings of the IEEE/CVF Winter Conference on Applications of Computer Vision*, pp. 1287–1297, 2024.
- [11] A. He, K. Wang, T. Li, W. Bo, H. Kang, and H. Fu, "Progressive multiscale consistent network for multiclass fundus lesion segmentation," *IEEE transactions on medical imaging*, vol. 41, no. 11, pp. 3146–3157, 2022.
- [12] J. Ruan, M. Xie, J. Gao, T. Liu, and Y. Fu, "Ege-unet: an efficient group enhanced unet for skin lesion segmentation," in *International Conference on Medical Image Computing and Computer-Assisted Intervention*, pp. 481–490, Springer, 2023.
- [13] N. Ibtchaz and D. Kihara, "Acc-unet: A completely convolutional unet model for the 2020s," in *International Conference on Medical Image Computing and Computer-Assisted Intervention*, pp. 692–702, Springer, 2023.
- [14] A. Vaswani, N. Shazeer, N. Parmar, J. Uszkoreit, L. Jones, A. N. Gomez, L. Kaiser, and I. Polosukhin, "Attention is all you need," *Advances in neural information processing systems*, vol. 30, 2017.
- [15] A. Dosovitskiy, L. Beyer, A. Kolesnikov, D. Weissenborn, X. Zhai, T. Unterthiner, M. Dehghani, M. Minderer, G. Heigold, S. Gelly, et al., "An image is worth 16x16 words: Transformers for image recognition at scale," *arXiv preprint arXiv:2010.11929*, 2020.
- [16] F. Shamschad, S. Khan, S. W. Zamir, M. H. Khan, M. Hayat, F. S. Khan, and H. Fu, "Transformers in medical imaging: A survey," *Medical Image Analysis*, p. 102802, 2023.
- [17] A. He, K. Wang, T. Li, C. Du, S. Xia, and H. Fu, "H2former: An efficient hierarchical hybrid transformer for medical image segmentation," *IEEE Transactions on Medical Imaging*, 2023.
- [18] A. Hatamizadeh, Y. Tang, V. Nath, D. Yang, A. Myronenko, B. Landman, H. R. Roth, and D. Xu, "Unetr: Transformers for 3d medical image segmentation," in *Proceedings of the IEEE/CVF winter conference on applications of computer vision*, pp. 574–584, 2022.
- [19] Z. He, M. Unberath, J. Ke, and Y. Shen, "Transnuseg: A lightweight multi-task transformer for nuclei segmentation," in *International Conference on Medical Image Computing and Computer-Assisted Intervention*, pp. 206–215, Springer, 2023.
- [20] J. Chen, Y. Lu, Q. Yu, X. Luo, E. Adeli, Y. Wang, L. Lu, A. L. Yuille, and Y. Zhou, "Transunet: Transformers make strong encoders for medical image segmentation," *arXiv preprint arXiv:2102.04306*, 2021.
- [21] J. Yu, X. He, J. Qin, W. Zhang, J. Xiang, and W. Zhao, "Transunet: A new decoder of transunet for medical image segmentation," in *2023 IEEE International Conference on Bioinformatics and Biomedicine (BIBM)*, pp. 2338–2341, IEEE, 2023.
- [22] Z. Liu, Y. Lin, Y. Cao, H. Hu, Y. Wei, Z. Zhang, S. Lin, and B. Guo, "Swin transformer: Hierarchical vision transformer using shifted windows," in *Proceedings of the IEEE/CVF international conference on computer vision*, pp. 10012–10022, 2021.
- [23] F. Zhang, A. Panahi, and G. Gao, "Fsanet: Frequency self-attention for semantic segmentation," *IEEE Transactions on Image Processing*, 2023.
- [24] Y. Zhou, J. Huang, C. Wang, L. Song, and G. Yang, "Xnet: Wavelet-based low and high frequency fusion networks for fully-and semi-supervised semantic segmentation of biomedical images," in *Proceedings of the IEEE/CVF International Conference on Computer Vision*, pp. 21085–21096, 2023.
- [25] K. Simonyan and A. Zisserman, "Very deep convolutional networks for large-scale image recognition," *arXiv preprint arXiv:1409.1556*, 2014.
- [26] S. Min, X. Zhang, and S. Wang, "Bfp-net: Boundary feature pyramid for medical image segmentation," in *2023 IEEE International Conference on Bioinformatics and Biomedicine (BIBM)*, pp. 1362–1367, IEEE, 2023.
- [27] X. Huang, J. Huang, S. Wang, Y. Wei, D. An, and J. Liu, "Polyp2former: Boundary guided network based on transformer for polyp segmentation," in *2023 IEEE International Conference on Bioinformatics and Biomedicine (BIBM)*, pp. 1971–1976, IEEE, 2023.
- [28] S. Yang, M. Jin, L. Wang, C. Lu, Y. Meng, D. Yan, Z. Huang, and J. Xu, "Medical image segmentation using dual branch networks with embedded attention mechanism," in *2023 IEEE International Conference on Bioinformatics and Biomedicine (BIBM)*, pp. 1620–1626, IEEE, 2023.
- [29] S. Woo, J. Park, J.-Y. Lee, and I. S. Kweon, "Cbam: Convolutional block attention module," in *Proceedings of the European conference on computer vision (ECCV)*, pp. 3–19, 2018.
- [30] N. Codella, V. Rotemberg, P. Tschandl, M. E. Celebi, S. Dusza, D. Gutman, B. Helba, A. Kallou, K. Liopyris, M. Marchetti, et al., "Skin lesion analysis toward melanoma detection 2018: A challenge hosted by the international skin imaging collaboration (isic)," *arXiv preprint arXiv:1902.03368*, 2019.
- [31] W. Al-Dhabyani, M. Gomaa, H. Khaled, and A. Fahmy, "Dataset of breast ultrasound images," *Data in brief*, vol. 28, p. 104863, 2020.
- [32] Z. Zhou, Y. Chen, A. He, X. Que, K. Wang, R. Yao, and T. Li, "Nkut: Dataset and benchmark for pediatric mandibular wisdom teeth segmentation," *IEEE Journal of Biomedical and Health Informatics*, 2024.
- [33] I. Loshchilov and F. Hutter, "Decoupled weight decay regularization," in *International Conference on Learning Representations*, 2018.
- [34] F. Milletari, N. Navab, and S.-A. Ahmadi, "V-net: Fully convolutional neural networks for volumetric medical image segmentation," in *2016 fourth international conference on 3D vision (3DV)*, pp. 565–571, IEEE, 2016.
- [35] H. Zhao, J. Shi, X. Qi, X. Wang, and J. Jia, "Pyramid scene parsing network," in *Proceedings of the IEEE conference on computer vision and pattern recognition*, pp. 2881–2890, 2017.
- [36] L.-C. Chen, Y. Zhu, G. Papandreou, F. Schroff, and H. Adam, "Encoder-decoder with atrous separable convolution for semantic image segmentation," in *Proceedings of the European conference on computer vision (ECCV)*, pp. 801–818, 2018.
- [37] H. Cao, Y. Wang, J. Chen, D. Jiang, X. Zhang, Q. Tian, and M. Wang, "Swin-unet: Unet-like pure transformer for medical image segmentation," in *European conference on computer vision*, pp. 205–218, Springer, 2022.
- [38] G. Xu, X. Leng, C. Li, X. He, and X. Wu, "Mgfuseseg: Attention-guided multi-granularity fusion for medical image segmentation," in *2023 IEEE International Conference on Bioinformatics and Biomedicine (BIBM)*, pp. 3587–3594, IEEE, 2023.
- [39] Z. Mirikharaji, K. Abhishek, A. Bissoto, C. Barata, S. Avila, E. Valle, M. E. Celebi, and G. Hamarneh, "A survey on deep learning for skin lesion segmentation," *Medical Image Analysis*, p. 102863, 2023.